

MULTI-MESSENGER DETECTION RATES AND DISTRIBUTIONS OF BINARY NEUTRON STAR MERGERS AND THEIR COSMOLOGICAL IMPLICATIONS

JIMING YU,^{1,2†} HAORAN SONG³, SHUNKE AI⁴, HE GAO³, FAYIN WANG^{5,6}, YU WANG^{1,2}, YOUJUN LU^{7,8}, WENJUAN FANG^{1,2}, AND WEN ZHAO^{1,2‡}

¹ CAS KEY LABORATORY FOR RESEARCHES IN GALAXIES AND COSMOLOGY, DEPARTMENT OF ASTRONOMY, UNIVERSITY OF SCIENCE AND TECHNOLOGY OF CHINA, CHINESE ACADEMY OF SCIENCES, HEFEI, ANHUI 230026, CHINA; [†] YJM8012@MAIL.USTC.EDU.CN, [‡] WZHAO7@USTC.EDU.CN

² SCHOOL OF ASTRONOMY AND SPACE SCIENCE, UNIVERSITY OF SCIENCE AND TECHNOLOGY OF CHINA, HEFEI, 230026, CHINA

³ DEPARTMENT OF ASTRONOMY, BEIJING NORMAL UNIVERSITY, BEIJING 100875, CHINA

⁴ DEPARTMENT OF PHYSICS AND ASTRONOMY, UNIVERSITY OF NEVADA LAS VEGAS, LAS VEGAS, NV 89154, USA

⁵ SCHOOL OF ASTRONOMY AND SPACE SCIENCE, NANJING UNIVERSITY, NANJING 210093, CHINA

⁶ KEY LABORATORY OF MODERN ASTRONOMY AND ASTROPHYSICS (NANJING UNIVERSITY), MINISTRY OF EDUCATION, CHINA

⁷ CAS KEY LABORATORY FOR COMPUTATIONAL ASTROPHYSICS, NATIONAL ASTRONOMICAL OBSERVATORIES, CHINESE ACADEMY OF SCIENCES, BEIJING, 100101, CHINA

⁸ SCHOOL OF ASTRONOMY AND SPACE SCIENCE UNIVERSITY OF CHINESE ACADEMY OF SCIENCES, BEIJING, 100049, CHINA

Draft version May 31, 2021

ABSTRACT

The gravitational-wave (GW) events, produced by the coalescence of binary neutron-stars (BNS), can be treated as the standard sirens to probe the expansion history of the Universe, if their redshifts could be determined from the electromagnetic observations. For the high-redshift ($z \gtrsim 0.1$) events, the short γ -ray bursts (sGRBs) and the afterglows are always considered as the primary electromagnetic counterparts. In this paper, by investigating various models of sGRBs and afterglows, we discuss the rates and distributions of BNS mergers' multi-messenger observations with GW detectors in second-generation (2G), 2.5G, 3G era with the detectable sGRBs and the afterglows. For instance, for Cosmic Explorer GW detector, the rate is about (300-3500) per year with GECAM-like detector for γ -ray emissions and LSST/WFST detector for optical afterglows. In addition, we find these events have the redshifts $z \lesssim 2$ and the inclination angles $i \lesssim 20^\circ$. These results justify the rough estimation in previous works. Considering these events as standard sirens to constrain the equation-of-state parameters of dark energy w_0 and w_a , we obtain the potential constraints of $\Delta w_0 \approx 0.02 - 0.05$ and $\Delta w_a \approx 0.1 - 0.4$.

1. INTRODUCTION

The discoveries of dozens of gravitational-wave (GW) signals produced by the inspiral and merger of compact binary systems (Abbott et al. 2016a,b,c,d, 2017a,b,c,e, 2019, 2020a,b,c,d) mark the opening of the era of GW astronomy. Since one can measure the luminosity distance of the GW source without any relying on a cosmic distance ladder (Schutz 1986), if the source's redshift can be measured independently, this kind of GW events can be treated as standard sirens to measure various cosmology parameters (Holz & Hughes 2005; Sathyaprakash et al. 2010; Zhao et al. 2011; Yan et al. 2020; Wang et al. 2020). On 2017 August 17, a GW event (GW170817) produced by a binary neutron star (BNS) system, together with a γ -ray burst (GRB 170817A) are observed (Abbott et al. 2017a,e; Goldstein et al. 2017; Savchenko et al. 2017). With the identification of their host galaxy, NGC 4993 (Arcavi 2017; Coulter et al. 2017; Soares-Santos et al. 2017; Tanvir et al. 2017; Valenti et al. 2017), advanced LIGO and Virgo collaborations (LVC) gave the first constraint on Hubble constant from standard sirens, $H_0 = 70^{+12.0}_{-8.0}$ km s⁻¹ Mpc⁻¹ with 68.3% confidence level (LIGO Collaboration et al. 2017). Many recent works also discussed the Hubble constant measurement through standard sirens (Chen et al. 2018; Fishbach et al. 2019; Soares-Santos et al. 2019; Mortlock et al. 2019; Gray et al. 2020; Yu et al. 2020).

Accurate measurement of luminosity distance d_L is crucial to standard sirens. Building more or more advanced detectors will improve the d_L measurement of the GW detection. At the same time, this will increase the redshift detection limit of GW signals, so GW standard sirens can be used to study the evolution of the high-redshift Universe. In the near fu-

ture, KAGRA (Abbott et al. 2018) and LIGO-India (Unnikrishnan 2013), will be built. Together with two advanced LIGO (aLIGO) and Virgo, there will be a network of five second-generation (2G) ground-based laser interferometer GW detectors. In LIGO Scientific Collaboration (2016), a modest cost upgrade of aLIGO, named LIGO A+, is proposed. Looking forward, two 3G detectors, including Einstein Telescope (ET) (Punturo et al. 2010; Abernathy et al. 2011) and Cosmic Explorer (CE) (Abbott et al. 2017f; Dwyer et al. 2015) are also under consideration.

The measurement of redshift is also an important task to standard sirens. One of the main methods is by observing their electromagnetic (EM) counterparts. The mergers of BNS and neutron star-black holes (NSBHs) are believed to create short GRBs (Paczynski 1986; Eichler et al. 1989; Narayan et al. 1992; Rosswog 2013) and kilonovae (Li & Paczyński 1998; Rosswog 2005; Tanvir et al. 2013; Metzger 2017). From the afterglow of GRBs or kilonovae, one can measure the GW source's redshift. Usually, the afterglows of GRB are with a much narrower observation angle but a larger redshift range (Berger 2014). Therefore, the observations of afterglows are more important for the standard sirens with high redshift.

In this work, we assume the jet profile obtained from the GRB170817A is quasi-universal for all BNS mergers and perform Monte Carlo simulations to estimate the magnitudes of their GW signals, GRB counterparts and afterglows. We select the samples that can be triggered by both GW interferometers and EM telescopes, and treat them as standard sirens. We get the standard sirens' rates and their distributions of redshifts and inclination angles. Moreover, we use these samples of standard sirens, combined with the method mentioned in Sathyaprakash et al. (2010) and Zhao et al. (2011), to discuss

the implications for dark energy parameters constraining by 3G GW interferometers.

This paper is organized as follows. In Sec. 2, we show the BNS samples used in this work. We introduce the detector response and the Fisher information matrix in Sec. 3. The jet profile of GRB170817A, the observation abilities of γ -ray detectors and optical telescopes we used are mentioned in Sec. 4. We estimate the detectability of BNS mergers' GW signals, GRB counterparts, afterglows, and discuss the implications of dark energy parameters constraints in Sec. 5. As a supplement, we discuss several alternative models for the EM counterparts in Sec. 6. In the end, we summarize our results in Sec. 7.

Throughout the paper, we choose the unit with $c = G = 1$, where G is the Newtonian gravitational constant and c is the speed of light in vacuum. We adopt the standard Λ CDM model with following parameters $H_0 = 67.8 \text{ km s}^{-1} \text{ Mpc}^{-1}$, $\Omega_m = 0.308$, $\Omega_\Lambda = 0.682$ (Planck Collaboration XIII 2016).

2. BNS SAMPLES

The event rate of BNS mergers with redshift z could be estimated as

$$N(z)dz = \frac{R_{\text{BNSmergers},0} \times f(z)}{1+z} \frac{dV(z)}{dz} dz, \quad (1)$$

where $R_{\text{BNSmergers},0}$ is the local BNS merger rate and we set it as $R_{\text{BNSmergers},0} = 80 - 810 \text{ Gpc}^{-3} \text{ yr}^{-1}$ in this work (Abbott et al. 2020e). $f(z)$ is the dimensionless redshift distribution function and $dV(z)/dz$ is the differential comoving volume, which is given by

$$\frac{dV(z)}{dz} = \frac{4\pi c}{\mathcal{H}(z)} \chi^2(z), \quad (2)$$

where $\chi(z)$ is the comoving distant, $\mathcal{H}(z)$ is the conformal Hubble parameter with redshift.

The dimensionless redshift distribution function $f(z)$ depends on the initial distribution of the BNS system and their delay time from generation to merger. Here, we first assume the initial distribution follows the star formation rate (SFR). We adopt the model derived by Yuksel et al. (2008):

$$\text{SFR}(z) \propto \left[(1+z)^{3.4\eta} + \left(\frac{1+z}{5000} \right)^{-0.3\eta} + \left(\frac{1+z}{9} \right)^{-3.5\eta} \right]^{1/\eta}, \quad (3)$$

with $\eta = -10$ and in units of $M_\odot \text{ Gpc}^{-3} \text{ yr}^{-1}$. For delay time, we use the log-normal distribution model (Wanderman & Pirran (2015)). In this module, the delay time τ has the distribution

$$P(\tau)d\tau = \frac{1}{\sqrt{2\pi}\sigma} \exp \left[-\frac{(\ln \tau - \ln t_d)^2}{2\sigma^2} \right] d\tau, \quad (4)$$

with $t_d = 2.9 \text{ Gyr}$ and $\sigma = 0.2$. The distribution of BNS merger samples can be integrated from Eq. (3) and Eq. (4)

$$f(z(t_0)) = \int \text{SFR}(z(t_0 - \tau)) P(\tau) d\tau. \quad (5)$$

The range of the initial distribution is from 0 to 7, with the same upper limit with Yuksel et al. (2008). So, we can get the BNS merger samples with the redshift distribution of Eq. (1). Their distribution is isotropic. As the component masses m_1 and m_2 , we choose a normal distribution $N(\mu = 1.32M_\odot, \sigma = 0.11M_\odot)$ for simulation, which following the observationally deviation distribution of galactic BNS

system (Kiziltan et al. 2013). We denote the inclination angle between the binary's orbital angular momentum and the line of sight as ι . The distribution of ι is proportional to $\sin \iota$. All of the BNS mergers in our simulation are non-spinning systems.

3. GW DETECTION

In this work, we mainly consider the network with N_d GW detectors and denote their spatial locations as \mathbf{r}_I with $I = 1, 2, \dots, N_d$. Here, we make an approximation that each detector has spatial size much smaller than the GW wavelength. It is worth noting that for 3G detectors, this approximation would introduce significant biases in localization (Essick et al. 2017). Therefore, the frequency-dependent responses should be considered in the real localization. In the Fig. 5 of Essick et al. (2017), the results of localization with/without this approximation are showed. Beyond the bias between them, they have similar errors. Since we concentrate on the error estimate in this work, this bias is unimportant and has little impact on our results. For the I -th detector, the response to an incoming GW signal traveling in direction \mathbf{n} could be written as a linear combination of two wave polarizations,

$$d_I(t) = F_I^+ h_\times(t) + F_I^\times h_+(t). \quad (6)$$

The I_{th} detector's beam-pattern function is decided by the source's right ascension (RA) α , declination (DEC) δ , the polarization angle ψ , the position and the orientation of interferometers's arms. In this paper, we consider the 2G interferometers LIGO (Livingston), LIGO (Handford), Virgo, KAGRA, LIGO-India and 3G interferometers ET, CE and an assumed CE-type detector. Our pervious paper, Yu et al. (2020), listed the parameters of these interferometers, which are also mentioned in Jaranowski et al. (1998), Blair et al. (2015) and Vitale & Evans (2017). For LIGO (Livingston), LIGO (Handford), Virgo, KAGRA, LIGO-India, we use the noise curve of the designed level for advanced LIGO (aLIGO) and A+ (LIGO Scientific Collaboration 2016). For CE in the U.S. and the assumed CE-type detector in Australia, we use the proposed noise curve in Abbott et al. (2017f) and Dwyer et al. (2015). And for ET, we consider the proposed ET-D project (Punturo et al. 2010; Abernathy et al. 2011). In this paper, we denote the network of LIGO (Livingston), LIGO (Handford) and Virgo with aLIGO-type of noise curve as LHV, and the network of five 2G interferometers as LHVIK. LHV A+ and LHVIK A+ are used to represent the networks with the noise curve of A+ type. CEET represents the network of CE in U.S. and ET in Europe and CE2ET is the network of two CE-type interferometers in U.S. and Australia, and one ET in Europe.

We adopt the restricted post-Newtonian (PN) approximation of the waveform for the non-spinning systems with only the waveforms in inspiralling stage (Sathyaprakash & Schutz 2009; Cutler et al. 1993; Blanchet 2002; Blanchet et al. 2002, 2004a,b; Blanchet & Iyer 2005; Damour et al. 2001; Erratum 2005; Itoh et al. 2001; Itoh & Futamase 2003; Itoh 2004a,b) in this paper. The terms h_+ and h_\times are depended on the mass ratio $\eta \equiv m_1 m_2 / (m_1 + m_2)^2$, the chirp mass $\mathcal{M}_c \equiv (m_1 + m_2) \eta^{3/5}$, the d_L , the ι , the merging time t_c and the merging phase ψ_c . Therefore, for a BNS merger, the response of interferometer depends on nine parameters, $\theta = \{\alpha, \delta, \psi, \iota, M, \eta, t_c, \phi_c, \log(d_L)\}$. Employing the nine-parameter Fisher matrix Γ_{ij} and marginalising over the over parameters, we derive the covariance matrix $(\Gamma^{-1})_{ij}$ for the nine parameters (Wen & Chen 2010). The signal-to-noise ratio (SNR) for

the GW signal can also be derived from the interferometer's response (See [Zhao & Wen \(2018\)](#) for details of Fisher matrix and SNR). In this work, we choose $\text{SNR} > 12$ as GW signal's threshold. Note that, in the realistic observation and analysis, various selection effects might induce the bias for the sources' parameters ([Chen et al. 2018](#); [Fishbach et al. 2019](#); [Mortlock et al. 2019](#); [Chen 2020](#)), which is beyond the scope of the current paper with Fisher matrix analysis. We leave it as a future work.

4. EM COUNTERPART DETECTION

4.1. γ -ray *Brust* detection

The observations of GW170817/GRB 170817A suggest it has a Gaussian-shaped jet profile ([Zhang & Mészáros 2002](#); [Troja et al. 2018](#); [Alexander et al. 2018](#); [Mooley et al. 2018](#); [Lazzati et al. 2018](#); [Ghirlanda et al. 2019](#))

$$E(t) = E_0 \exp\left(-\frac{t^2}{2t_c^2}\right) \quad (7)$$

for $t \leq t_w$, where E_0 is the on-axis equivalent isotropic energy, t_c is the characteristic angle of the core, t_w is the truncating angle of the jet. [Troja et al. \(2018\)](#) give the constraints on the jet with $t_c = 0.057^{+0.025}_{-0.023}$, $\log_{10} E_0 = 52.73^{+1.3}_{-0.75}$, $t_w = 0.62^{+0.65}_{-0.37}$. We assume all BNS mergers in our simulation has a relativistic jet with this profile. In order to convert this energy profile to the luminosity profile, we assume the burst duration $T_{90} \sim 2$ s ([Abbott et al. 2017d](#)) and the spectrum is flat with time during the burst, where T_{90} is defined as the duration of the period which 90% of the burst's energy is emitted. So, the γ -ray flux of each BNS mergers can be written as

$$F_\gamma = \frac{E_0 \eta_\gamma}{4\pi D_L^2 T_{90}} \exp\left(-\frac{t^2}{2t_c^2}\right), \quad (8)$$

where η_γ is the radiative efficiency and we adopt it as 0.1 for the bolometric energy flux in the 1 - 10^4 keV band. We assume the spectrum for all BNS-associated-GRBs follow the Band function

$$N(E) = A \begin{cases} \left(\frac{E}{100 \text{ keV}}\right)^\alpha \exp\left[-\frac{(2+\alpha)E}{E_p}\right], & E \leq \frac{(\alpha-\beta)E_p}{2+\alpha}, \\ \left(\frac{E}{100 \text{ keV}}\right)^\beta \left[\frac{(\alpha-\beta)E_p}{(2+\alpha)100 \text{ keV}}\right]^{\alpha-\beta} e^{\beta-\alpha}, & E \geq \frac{(\alpha-\beta)E_p}{2+\alpha}. \end{cases} \quad (9)$$

Here $N(E)$ is in units of photons $\text{cm}^{-2} \text{s}^{-1} \text{keV}^{-1}$ and E_p corresponds to the peak energy in the νF_ν spectra. We adopt the photon indices α and β as, -1 and -2.3 ([Preece et al. 2000](#)) below and above the peak energy E_p respectively. However, the bolometric isotropic luminosity L and the peak energy for GRB 170817A do not follow the E_p - L relation for short γ -ray bursts ([Zhang & Wang 2018](#)) and long γ -ray bursts ([Yonetoku et al. 2004](#)), which can be written as

$$\frac{L}{10^{52} \text{ erg s}^{-1}} = \left(2.34^{+2.59}_{-1.76}\right) \times 10^{-5} \left[\frac{E_p(1+z)}{1 \text{ keV}}\right]^{2.0 \pm 0.2}. \quad (10)$$

There is a profile proposed by [Ioka & Nakamura \(2019\)](#) that the peak energy E_p changes with ι with following relationship

$$E_p(\iota) = E_{p,0} \times (1 + \iota/t_c)^{-0.4}, \quad (11)$$

within the Gaussian structure jet framework, where $E_{p,0}$ is the peak energy that satisfies the Yonetoku relation. This profile makes the GRB170817a observations consistent with previous GRB observation.

With the peak energy and the Band function, we can get the effective sensitivity limit for various γ -ray detectors. Here we adopt the same setting as [Song et al. \(2019\)](#), the sensitivity for Fermi-GBM is adopted as $\sim 2 \times 10^{-7} \text{ erg s}^{-1} \text{ cm}^{-2}$ in 50 keV to 300 keV ([Meegan et al. 2009](#)), the sensitivity for GECAM is adopted as $\sim 1 \times 10^{-7} \text{ erg s}^{-1} \text{ cm}^{-2}$ in 50 keV to 300 keV ([Zhang et al. 2018](#)), the sensitivity for Swift-BAT and SVOM-ECLAIRS is adopted as $\sim 1.2 \times 10^{-8} \text{ erg s}^{-1} \text{ cm}^{-2}$ in 15 keV to 150 keV ([Gehrels et al. 2004](#); [Götz et al. 2014](#)), and the sensitivity for Einstein Probe (EP) is adopted as $\sim 3 \times 10^{-9} \text{ erg s}^{-1} \text{ cm}^{-2}$ in 0.5 keV to 4 keV ([Yuan et al. 2018](#)). Another important factor affecting the detection ability of the γ -ray detector is the size of its field of view. For Fermi-GBM, its field of view (FOV) covers about 3/4 of the whole sky and for GECAM, the field of view is about 4π . For other three detectors, their fields of view are much smaller. The factors are $\sim 1/9$ for Swift-BAT, $\sim 1/5$ for SVOM-ECLAIRS ([Chu et al. 2016](#)) and $\sim 1/11$ for EP compared with the whole sky. Note that, these γ -ray detectors might have no overlapped observational time with future 3G GW detector networks. However, we expect the similar or more powerful detectors in 3G era. So, for simplification, throughout this paper we only consider these γ -ray detectors for illustration.

4.2. Afterglows of γ -ray burst

The measurements of GRBs' redshift relies on the identification of their host galaxies and further optical observations. And the afterglow usually plays a crucial role in the host galaxy identification. In this paper, we use the standard afterglow models ([Sari et al. 1998](#)) to estimate the afterglows on R band. The spectra and light curve are determined by the inclination angle ι , the half-opening angle θ_j , the total kinetic energy $E_j = (1 - \cos \theta_j)E_0$, the number density of the interstellar medium (ISM) n_0 , the magnetic field energy fraction ϵ_B , the accelerated electron energy fraction ϵ_e , the power-law index of shock-accelerated p , the luminosity distance d_L and the time after merger in unit of days t_j .

With adopting the convention notion $Q = 10^x Q_{x,s}$ for a adiabatic jet, the Lorentz factor is given by ([Sari et al. 1998](#))

$$\gamma(t) = 8.9(1+z)^{3/8} E_{j,51}^{1/8} n_0^{-1/8} \theta_{j,-1}^{-1/4} t_d^{-3/8}. \quad (12)$$

For an on-axis observer, a phenomenon named jet break is expected when γ drops below θ_j and the jet's material begin to spread sideways ([Sari et al. 1998](#); [Mészáros & Rees 1999](#)). At the jet break time, there will be a break in the afterglow's light curve. From Eq. (12), the jet break time t_j is given by

$$t_j = 0.82(1+z) E_{j,51}^{1/3} n_0^{-1/3} \theta_{j,-1}^2 \text{ days}. \quad (13)$$

At the jet-break time, there are two cases for flux density, $F_{\nu,j}$, the slow-cooling case ($\nu_m < \nu < \nu_c$) and the fast cooling case ($\nu_c < \nu$), where ν_m is the typical synchrotron frequency of the accelerated electrons with the minimum Lorentz and ν_c is the cooling frequency. In the slow-cooling case, $F_{\nu,j} \propto \nu^{-(p-1)/2}$, where we adopt $p = 2.2$ in this paper (the same as [Nakar et al. \(2002\)](#) and [Zou et al. \(2007\)](#)). While in the fast-cooling case, $F_{\nu,j} \propto \nu^{-p/2}$ ([Sari et al. 1998](#)).

For an on-axis observer, the light curve is divided into two power-law segments by the jet break time ([Sari et al. 1998](#)). We denote the temporal decay index of the flux density $F_{\nu,0}(t)$ in the time as α_1 and α_2 , which represent the time before and after t_j , respectively. The index α_1 is $-(2-3p)/4$ in the fast cooling case and $-3(1-p)/4$ in the slow cooling case. When

$t > t_j$, the on-axis observer can only observe $\sim \theta_j^2 \gamma^2$ of the flux density in the isotropic fireball case. Since $\gamma(t) \propto t^{-3/8}$, we have $\alpha_2 = \alpha_1 + 3/4$.

For a point source moving at angle ι , the observed flux is (Granot et al. 2002)

$$F_\nu = \frac{L'_{\nu'}}{4\pi d_A^2} \left(\frac{\nu}{\nu'} \right), \quad (14)$$

where d_A is the angular distance, $L'_{\nu'}$ and ν' are the jet comoving frame spectral luminosity and frequency. For an off-axis observer (t, ν) at the angle ι and an on-axis observer (t_0, ν_0) at the angle 0, there are $t_0/t \approx \nu/\nu_0 = (1 - \beta)/(1 - \beta \cos \iota) \equiv a$, where $\beta = \sqrt{1 - 1/\gamma^2}$. And we obtain

$$F_\nu(t, \nu) = a^3 F_{\nu/a}(0, at). \quad (15)$$

Here we consider both fast and slow cooling cases, which are $\nu_c < \nu$ and $\nu_m < \nu < \nu_c$, respectively.

5. MULTI-MESSENGER OBSERVATION OF GW AND GRB

5.1. Detection rates

Since we find $z = 3$ has exceeded the detection limit of the GRB detectors in the simulations, we set it as the upper redshift limit and sampled 10^7 BNS mergers. However, this upper limit is too high for the 2G interferometers that the simulation became very inefficient with them. The upper detection limit with LHVIK A+ is about $z \sim 0.2$, so for the 2G interferometers, we resample them with $z \in (0, 0.3]$.

There are $\sim 3.4 \times 10^5$ BNS samples detected by ET and 5.1×10^6 detected by CE. For 2G GW detector networks LHV, LHVIK, LHV A+ and LHVIK A+, the numbers are 2.7×10^4 , 5.7×10^4 , 1.6×10^5 and 3.3×10^5 , respectively, with samples' $z \in (0, 0.3]$. The observation ability of A+ type network will improve several times even with less detectors. About 10-12% BNS mergers' GW signal observed by 2G GW detector networks could be triggered by γ -ray detector. For 3G detectors, the fractions are much lower because more events have high redshift.

We convert these numbers into rates per year, after multiplying the total rate of BNS mergers. Integrating Eq. (1), in $z \in (0, 0.3]$, the total rate is $1159\text{-}11736 \text{ yr}^{-1}$ and in $z \in (0\text{-}3]$, the total rate is $6.9 \times 10^4 - 7.0 \times 10^5 \text{ yr}^{-1}$. Due to the limited observation area of the γ -ray detectors, not all GRB events whose flux reaches the threshold count be observed. So the multi-messenger observation rates require a discount, FOV/Ω_0 , where Ω_0 is the solid angle of whole sky. Table 1 lists the observation rates per year with this discount. For LHV, the rate is 0.042-0.425 per year with Swift-BAT and 0.072-0.731 per year with SVOM-ECLAIRS. For GECAM and Fermi-GBM, the rates are a few times larger due to their much larger observation areas. The result of EP is slightly worse than Swift-BAT due to its smaller observation area, although it has better sensitivity. After adding two LIGO-type detectors, the rates of LHVIK are about twice as large as LHV. The future upgrade of aLIGO, A+ would increase these numbers by about five times. For 3G interferometers ET, their will be about $100 \sim 800$ multi-messenger observation rate with different γ -ray detectors if we adopt $810 \text{ Gpc}^{-3} \text{ yr}^{-1}$ as the local merger rate. The rates are much larger even only with one single interferometer. For another 3G interferometer CE, the rates are a few times larger compared with ET, since it has a further observation range. It is worth noting that we assume the GW and GRB detections are independent.

However, in the real situation, with a triggered GRB, one can search weaker GW signals. So the numbers in Table 1 might be slightly smaller compared to the actual situation.

We select the BNS samples that can be triggered by both GW interferometers and γ -ray detectors. We choose the result of GECAM as a representative and show their redshift distribution in Fig. 1. The redshift limits of LHV and LHVIK are around $z \sim 0.1$ and the the detection limit of LHVIK A+ can reach ~ 0.2 due to more sensitive detection capabilities. For 3G interferometers ET and CE, the redshift limits are $z \sim 1.0$ and $z \sim 2.5$, respectively.

As an important method for measuring redshift information, we also calculate the magnitude of GRB afterglows with the method mentioned in Subsection 4.2. We adopt $n_0 = 1 \text{ cm}^{-3}$, $p = 2.2$, $\epsilon_e = 0.1$, $\epsilon_B = 0.01$, $p = 2.2$, where they are the same as Nakar et al. (2002) and Zou et al. (2007). For the half opening angle, we consider three cases, $\theta_j = 5^\circ, 10^\circ, 15^\circ$. For off-axis samples, we calculate the afterglows' maximum R band magnitude M_R with different opening angles respectively. However, for on-axis GRB samples, their afterglows power-law decay with time and we cannot get their maximum M_R from their light curve, as showed in Fig. 2, so we denote the R band flux in the jet break time as M_R in this case, as a comparison with the off-axis samples.

Using the case of GECAM and $\theta_j = 10^\circ$ as an example, we show the distributions of standard sirens' redshift, inclination angle and the flux of afterglows in Fig. 3. From these figures, we can intuitively see the ι limit of multi-messenger observation. In very low redshift, there is a BNS sample with $\iota \sim 22^\circ$. This sample's inclination angle and redshift are very similar with GW170817. For samples with $z = 1$, the ι limit becomes to about 15° . Zhao et al. (2011) and Sathyaprakash et al. (2010) have roughly estimated the distribution of GW sources on the order of magnitude, which is about 1000 per year with inclination angle $\iota < 20^\circ$. These predictions are based on the \sim several $\times 10^5$ BNS rate per year within the horizon of ET, and $\sim 10^{-3}$ of them will have GRBs toward us. These estimates meet well with our result. We use the improved measurement of BNS merger rate from GW observations and give stronger constraints on the multi-messenger event rates. In the next subsection, we will use their methods, combined with our results of simulations, to show the potential of determination of dark energy by the 3G GW interferometers ET and CE. The design specification of LSST for 5σ depths for point sources in the r band is ~ 24.7 (Ivezić et al. 2019), which correspond to point sources and fiducial zenith observations. Due to the small inclination angles, all standard sirens have M_R brighter it. For 2.5-meter Wide Field Survey Telescope (WFST), the sigle-visit depth with a 30 s exposure time is $r \sim 22.8$. A small fraction of samples in the case of SVOM fainter than $r \sim 22.8$. If we consider a 300 s exposure time, the sigle-visit depth of WFST will reach $r \sim 24.1$ and all samples have M_R brighter than it. In other two choices of θ_j , their afterglows all reach the design depth of LSST and WFST. Therefore, we have assume all multi-messenger BNS events in our simulation have a detectable afterglow and we can measure their redshift from their afterglows.

In Fig. 4, we set the number density of ISM as $n_0 = 0.1 \text{ cm}^{-3}$ and $n_0 = 0.01 \text{ cm}^{-3}$ as a comparison, respectively. GRB surrounded by thinner ISM usually has a weaker afterglow. In the case of $n_0 = 0.01 \text{ cm}^{-3}$, a small fraction of afterglows are fainter than the design depth of LSST and WFST. In that case, the measurement of GRBs' redshift seems difficult

and further discussion is needed.

5.2. Determination of Dark Energy

In the last two decades, the accelerated expansion of the universe has been confirmed by a series of observations (Kowalski et al. 2008; Hicken et al. 2009; Komatsu et al. 2009; Eisenstein et al. 2005; Percival et al. 2007, 2010; Schrabback et al. 2010; Kilbinger et al. 2009). Various models of dark energy have been proposed to explain it (see Copeland et al. (2006) for a review). In order to understand the physical properties of dark energy, it is important to measure its equation of state (EOS). In Sathyaprakash et al. (2010) and Zhao et al. (2011), the new method of measuring the dark energy EOS using GW standard sirens was proposed. Zhao & Wen (2018) compared the results of GW detector networks with 1000 face-on BNS sources, with baryon acoustic oscillations (BAO) method, and Type Ia supernovas (SNIa) method, and found that by the 3G GW detector networks, the constraints of dark energy parameters are similar with the SNIa and BAO methods. In this subsection, we will discuss these constraints with a quantitatively distributed BNS sample.

Similar to Zhao et al. (2011), we adopt a phenomenological form for EOS parameter w as a function of redshift (Chevallier & Polarski 2001)

$$w(z) \equiv \frac{p_{\text{de}}}{\rho_{\text{de}}} = w_0 + w_a \frac{z}{1+z}, \quad (16)$$

where p_{de} is the pressure of dark energy and ρ_{de} is the energy density. The parameter w_0 represent the present EOS and w_a represent the evolution with redshift. In the Λ CDM model, the relation of $d_L - z$, is determined by $(H_0, \Omega_m, \Omega_k, w_0, w_a)$ together (Weinberg 2008). So if the $d_L - z$ relation can be measured from a series of multi-messenger observations, the set of these 5 parameters would have chance to be constrain. However, due to the strong degeneracy between the background parameters $(H_0, \Omega_m, \Omega_k)$ and the dark energy parameter (w_0, w_a) , the constraints of full parameters set seems unrealistic (Zhao et al. 2011). The same problem also happens in other methods for dark energy detection (e.g., SNIa and BAO methods) (Albrecht et al. 2006; Zhao et al. 2011). A general way to break this degeneracy is to combine the result with the CMB data, which are sensitive to the background parameters $(H_0, \Omega_m, \Omega_k)$, and provide the necessary complement to the GW data. It has also been discovered in (Zhao et al. 2011) that taking the Planck CMB observation as a prior is nearly equivalent to treating the parameters $(H_0, \Omega_m, \Omega_k)$ as known in the data analysis. Thus, similar to Zhao & Wen (2018), Zhao et al. (2018) and Yan et al. (2020), in this article we use the GW data to constrain the dark energy parameters (w_0, w_a) only.

To estimate the errors of (w_0, w_a) , we consider a Fisher matrix F_{ij} for a collection of N BNS mergers that follows our sample distribution, which is given by (Zhao et al. 2011)

$$F_{ij} = \sum_{k=1}^N \frac{\partial \ln d_L(z_k)}{\partial p_i} \frac{\partial \ln d_L(z_k)}{\partial p_j} \frac{1}{(\delta d_L/d_L(\hat{\gamma}_k, z_k))^2}, \quad (17)$$

where i and j run from 1 to 2, denoting the free parameter w_0 and w_a , and $\hat{\gamma}$ represents the angle $(\alpha, \delta, \iota, \psi)$. The distance error $\delta d_L/d_L$ have two components: the instrument error $\Delta d_L/d_L$, and the error caused by the effects of weak lensing. We denote this error as $\tilde{\Delta} d_L/d_L$ and assume it satisfies $\tilde{\Delta} d_L/d_L = 0.05z$ (Sathyaprakash et al. 2010; Zhao et

al. 2011; Zhao & Wen 2018; Wang & Wang 2019). So the total distance error could be estimated from $\delta d_L/d_L = \sqrt{(\Delta d_L/d_L)^2 + (\tilde{\Delta} d_L/d_L)^2}$. Similar to Gupta et al. (2019) and Zhao & Santos (2019), in order to evaluate Δd_L for each event, we assume the parameters (α, δ, ι) are constrained well by γ -ray observation and consider a Fisher matrix of six parameters, $(\psi, M, \eta, t_c, \phi_c, \log d_L)$. This scenario is possible as we have already have seen in the case of GW170817. The sky position of GW170817 was constrained by finding the host galaxy NGC 4993 (LSC et al. 2017) whereas the inclination angle was constrained from the X-ray and ultraviolet observations (Evans et al. 2017). In Fig. 5 we use the case of GECAM as a representative case and show the distribution of samples instrument errors with two single 3G GW detectors, ET and CE. There is an obvious cutoff around $\Delta \log d_L \sim 0.08$, since the instrument errors have a strong correlation with SNR and we choose SNR= 12 as the threshold.

The uncertainties of cosmological parameters are given by $\Delta w_0 = (F^{-1})_{11}$ and $\Delta w_a = (F^{-1})_{22}$. If the statistical errors are dominant, the uncertainties of w_0 and w_a are proportional to $1/\sqrt{N}$. In Table 2, we list the 68.3% ($1-\sigma$) uncertainties of w_0 and w_a marginalized over other parameter with one year's multi-messenger observation. Also, to estimate the goodness of parameter constraints, we list the figure of merit (FoM) (Albrecht et al. 2006) in Table 2, which is written as

$$\text{FoM} = [\text{Det } C(w_0, w_a)]^{-1/2}, \quad (18)$$

where $C(w_0, w_a)$ is the covariance matrix of w_0 and w_a . With the large observation area, the results of GECAM and Fermi-GBM are much better than other γ -ray detectors. For GECAM and CE, we obtain $\Delta w_0 = 0.016 - 0.051$, $\Delta w_a = 0.119 - 0.380$ and FoM = 171 - 1732, for Fermi-GBM, the results are $\Delta w_0 = 0.020 - 0.065$, $\Delta w_a = 0.157 - 0.499$ and FoM = 100 - 1009. These results are comparable with the detection abilities of SNIa and BAO methods in the long-term (Stage IV) projects, which are FoM ~ 300 for SNIa method and FoM ~ 100 for BAO method (Albrecht et al. 2006; Zhao et al. 2011). We can also see that the ET has poor ability of constraining w_0 and w_a due to its low observation limit. In Fig. 6, the corresponding two-dimensional $1-\sigma$ uncertainty contours of these multi-messenger observations with ET and CE are plotted, and in each figure, we compare the results with four different γ -ray detectors. For the case of GECAM, the constraints of dark energy parameters are significantly more stringent than other three γ -ray detectors due to its large observation areas. The results of CEET and CE2ET are not showed here because their shapes are very similar with the results with CE. Our results roughly match the results of Zhao & Wen (2018), but using a much more quantitative BNS sample.

6. EFFECT OF ALTERNATIVE MODELS FOR EM COUNTERPARTS

In previous discussions, we assume all BNS mergers have a Gaussian-shaped jet profile in the form of Eq. (7). In Abbott et al. (2017e), other two jet profiles are used to explain the observed properties of GRB 170817A, uniform top-hat jets and 'cocoon' emission model (Lazzati et al. 2017). However, the compact radio emission observations favor the structured jet profile (Ghirlanda et al. 2019). Therefore, in this article, we will not consider these two models. Meanwhile, to combine GRB 170817A and other SGRBs, Tan & Yu (2018) produce a two-Gaussian profile,

$$L_{\text{iso}}(\iota) = L_{\text{on}} \left[\exp\left(-\frac{\iota^2}{2\theta_{\text{in}}^2}\right) + C \exp\left(-\frac{\iota^2}{2\theta_{\text{out}}^2}\right) \right], \quad (19)$$

| | Swift-BAT | SVOM-ECLAIRS | GECAM | Fermi-GBM | EP |
|----------|-------------|--------------|--------------|--------------|-------------|
| LHV | 0.042-0.425 | 0.072-0.731 | 0.278-2.820 | 0.198-2.001 | 0.029-0.297 |
| LHVIK | 0.084-0.856 | 0.146-1.474 | 0.553-5.598 | 0.394-3.985 | 0.058-0.593 |
| LHV A+ | 0.217-2.200 | 0.374-3.789 | 1.370-13.870 | 0.962-9.741 | 0.148-1.504 |
| LHVIK A+ | 0.445-4.505 | 0.766-7.757 | 2.743-27.769 | 1.907-19.305 | 0.301-3.046 |
| ET | 17.0-172.0 | 29.2-296.1 | 80.6-815.6 | 49.9-504.9 | 10.7-108.5 |
| CE | 98.1-993.0 | 168.9-1710.0 | 342.1-3463.5 | 188.4-1907.4 | 58.1-587.9 |

TABLE 1
THE MULTI-MESSENGER OBSERVATION RATES (WITH THE UNIT OF YEAR⁻¹) FOR BNS MERGERS WITH DIFFERENT γ -RAY DETECTORS AND GW DETECTORS.

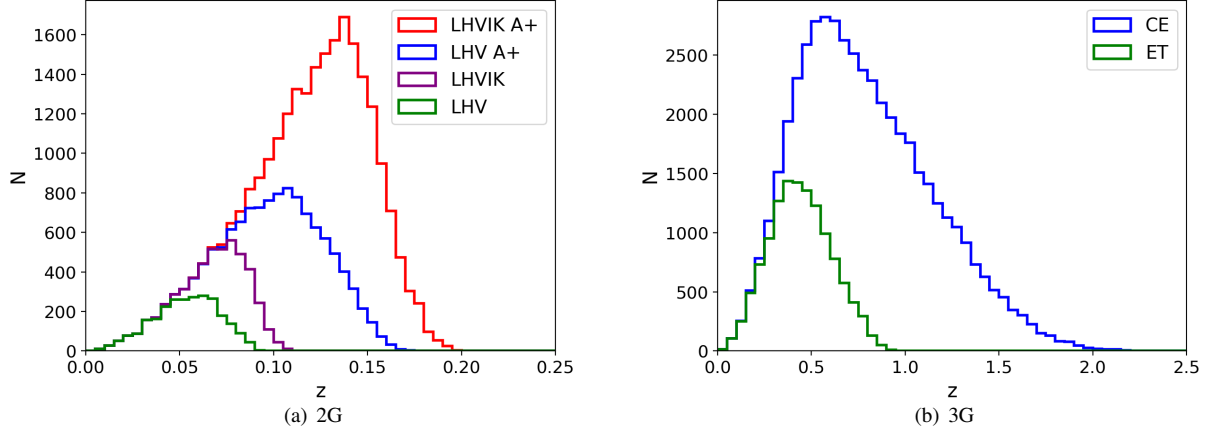


FIG. 1.— The number distributions of samples that can be both triggered by GW interferometers and GECAM.

| | | Swift-BAT | SVOM-ECLAIRS | GECAM | Fermi-GBM | EP |
|--------------|-------|-------------|--------------|--------------|--------------|-------------|
| Δw_0 | ET | 0.129-0.412 | 0.099-0.314 | 0.057-0.181 | 0.070-0.222 | 0.160-0.510 |
| | CE | 0.034-0.107 | 0.026-0.082 | 0.016-0.051 | 0.020-0.065 | 0.043-0.136 |
| | CEET | 0.032-0.104 | 0.025-0.079 | 0.015-0.049 | 0.020-0.062 | 0.041-0.131 |
| | CE2ET | 0.028-0.090 | 0.022-0.069 | 0.013-0.042 | 0.017-0.054 | 0.036-0.114 |
| Δw_a | ET | 1.173-3.734 | 0.894-2.846 | 0.531-1.690 | 0.664-2.114 | 1.462-4.652 |
| | CE | 0.237-0.754 | 0.181-0.575 | 0.119-0.380 | 0.157-0.499 | 0.303-0.966 |
| | CEET | 0.228-0.727 | 0.174-0.554 | 0.115-0.366 | 0.151-0.481 | 0.293-0.931 |
| | CE2ET | 0.198-0.630 | 0.151-0.480 | 0.100-0.318 | 0.132-0.419 | 0.254-0.808 |
| FoM | ET | 2.4-24.4 | 4.1-42.0 | 11.7-118.8 | 7.4-75.0 | 1.5-15.6 |
| | CE | 42.5-430.5 | 73.2-741.3 | 171.1-1732.0 | 99.7-1009.1 | 26.0-263.0 |
| | CEET | 45.7-462.9 | 78.7-797.1 | 183.7-1860.3 | 107.0-1083.8 | 27.2-282.7 |
| | CE2ET | 60.4-611.4 | 104.0-1052.9 | 241.7-2447.6 | 140.6-1423.9 | 36.8-372.9 |

TABLE 2
THE $1 - \sigma$ CONSTRAINTS OF Δw_0 AND Δw_a BY ONE YEAR'S JOINT OBSERVATIONS WITH DIFFERENT GW INTERFEROMETERS AND γ -RAY DETECTORS. THE FoM IN EACH CASE IS ALSO SHOWN.

where L_{on} , θ_{in} , θ_{out} , C are four free parameters, with $\theta_{out} = 10\theta_{in}$ and $C \ll 1$. We choose the $\theta_{in} = 2^\circ$ Model as example. The multi-messenger observation rates with this model are showed in Table 3. For 2G GW network, the rates with Swift-BAT and SVOM are a few times larger than the case of Gaussian jet profile, since more GRBs in this model have peak energy in Swift-BAT and SVOM's flux band. Other rates are roughly same. For 3G interferometers, the rates are about half compared with Table 1, since two-Gaussian profile is narrower around $\iota = 0^\circ$.

In Sec. 2, we use the log-normal distribution time delay model. In Sun et al. (2015), the authors investigated it with other two models, i. e. Gaussian delay model (Virgili et al. 2011) and power-law delay model (Sun et al. 2015). The power-law delay model is not supported by the SGRB data

(Virgili et al. 2011). Therefore, we concentrate on the difference between Gaussian and log-normal delay models here. The $f(z)$ mentioned in Eq. (5) with these two models are painted in Fig. 7 and the observation rates with Gaussian delay model are showed in Table 4. While $z < 0.5$, the distributions are almost same. So for 2G GW networks, the multi-messenger observation rates are also almost same. However, while for high redshift, the Gaussian delay model predicts a larger number of BNS samples, so the rates in the case of 3G interferometers, especially for CE, are larger than log-normal delay model.

Another issue that needs to be discussed is, GW190425 (Abbott et al. 2020a), a compact binary coalescence with total mass $\sim 3.4 M_\odot$ does not fit in with the BNS mass distribution assumed in our work. In order to cover the GW190425-

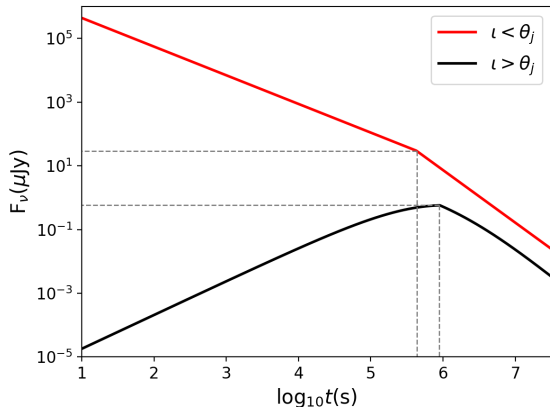


FIG. 2.— This figure show the light curve of on-axis and off-axis afterglows. The red and black curves are the cases of on-axis afterglow with $\iota = 5^\circ$ and off-axis afterglow with $\iota = 15^\circ$, respectively. Other parameters in these two cases are same, with $E_0 = 10^{52.73}$ erg, $z = 1$ and $\theta_j = 10^\circ$.

type systems, we follow the same setting as Abbott et al. (2020e), assume a uniform mass distribution between $1 M_\odot$ and $2.5 M_\odot$. In Fig. 8, we compare the redshift distributions of BNS samples which can be both triggered by GW interferometers and GECAM with two BNS mass distributions. Due to the heavy BNS mergers considered, for 2G GW interferometers and ET, more and further BNS mergers can be observed. However, for CE, since the maximum observation distance exceeds the γ -ray detectors' and the dominant constraints come from GRB observations, the results of two mass distributions are very similar. In Table 5, the merger rates with other γ -ray detectors and GW interferometers are listed.

In this section, we discuss three different models as a comparison and predict the multi-messenger observation rates with each model. Following the method mentioned in Sec. 5.2, we calculate the constraints on w_0 and w_a through multi-messenger observations with these three models. In Fig. 9, we compare the corresponding two-dimensional $1 - \sigma$ uncertainty contours of Δw_0 and Δw_a with four models. The contours with two-Gaussian jet profile are larger than others due to smaller observation rates. In the case of ET and flat mass distribution, the constraints are better. And in other cases, the results are roughly similar.

7. CONCLUSIONS

The detection of GW170817 opens a door of multi-messenger observation. From the GW waveforms of these events, we could measure the sources' luminosities distances independently, without the comic distance ladder. If the redshifts of the sources could also be measured from other methods, this kind of GW events could be treated as the standard sirens to constrain cosmological parameters, such as Hubble constant, dark energy and so on. A direct way to measure the sources' redshifts is to find their host galaxies by the observation of their EM counterparts, such as GW170817.

In this paper, we discuss the multi-messenger observations of BNS mergers' GW and GRB signals. We find the network of the 2.5G network LHVIK A+ are expect to detect more than 3 multi-messenger signals per year with different γ -ray detectors, if the local merger rate is $810 \text{ Gpc}^{-3} \text{ yr}^{-1}$. And the upper redshift limit of these BNS samples is about 0.2. For the LHVIK or LHV A+, the numbers are about several times smaller than LHVIK A+. Most of the BNS mergers which

could be triggered by both GW interferometers and γ -ray detectors have $\iota \leq 22^\circ$, because of the limitation of the Gaussian jet profile. Only a few samples in very low redshift with inclination angles larger than 22° can be triggered by γ -ray detectors. For the 3G interferometer ET and CE, the number of the multi-messenger observation rates are tens to hundreds of times larger compared with LHVIK A+. The upper redshift limit for ET is ~ 1 and for CE, the upper limit is ~ 2.5 . We also find for the samples with z larger than 1.0, the requirements on the inclination angles become stricter, becoming less than 15° . The results of 3G GW detectors are in line with the magnitude estimates of BNS event rates in Sathyaprakash et al. (2010) and Zhao et al. (2011). BNS mergers' inclinations that can be observed by both GW and γ -ray detectors are almost all less than 22° , which also match these works' estimate.

Due to the high redshift upper limit of the multi-messenger observations with the 3G GW detectors, we discuss the implication for constraining dark energy parameters with BNS mergers. One year's observations of ET can constrain the EOS of cosmic dark energy with accuracies $\Delta w_0 \sim 0.06-0.18$ and $\Delta w_a \sim 0.5 - 1.7$ with GECAM. For CE, the results are much better, which are $\Delta w_0 \sim 0.02-0.05$ and $\Delta w_a \sim 0.1-0.4$. We also discuss the cases of 3G GW detector networks, CEET and CE2ET. The results of CEET are quite close to CE and the results of CE2ET have a $\sim 10-20\%$ progress. Therefore, the usage of 3G interferometers will provide an important method to help us understand the high-redshift Universe.

Note that, Belgacem et al. (2019) also estimated the multi-messenger observation rates, where the authors used a Gaussian structured jet profile with specific parameters and selected observed GRBs through their peak flux. In this work, we make a much more comprehensive and integrated analysis on this issue. We discuss a more general structured jet profile and calculate the spectrum of each GRB sample from the Band function, and integrate it in the band of different GRB detectors, instead of peak flux. Because of these, our predictions are several times larger than the results in Belgacem et al. (2019). In order to study the uncertainties in BNS samples and GRB jets, we discuss several alternative models. The two-Gaussian jet profile, the Gaussian time delay model and a flat BNS mass distribution are discussed as a supplement. The two-Gaussian jet profile model brings a narrower jet and a softer spectrum. The results of 2G GW networks and Swift-BAT/SVOM are ~ 4 times larger and the rates with 3G GW detectors are about half. The Gaussian delay time model predicts a larger BNS merger rate in high redshift and the results of 3G interferometers are slightly larger. The flat BNS mass distribution takes heavy BNS mergers into account, and the rates with ET have a $\sim 50\%$ increase. But for CE, due to the constraints from GRB observations, the rates are almost same. We also estimate the magnitudes of optical afterglows and find that, if the number density of ISM is 1 cm^{-3} , due to the low inclination angle, all multi-messenger events have optical afterglows that reach the single-visit depth of LSST and/or WFST.

This work is supported by the National Natural Science Foundation of China under Grant Nos. 11903030, 11773028, 11603020, 11633001, 11653002, the Strategic Priority Program of the Chinese Academy of Sciences (Grant No. XDB 23040100) and the Fundamental Research Funds for the

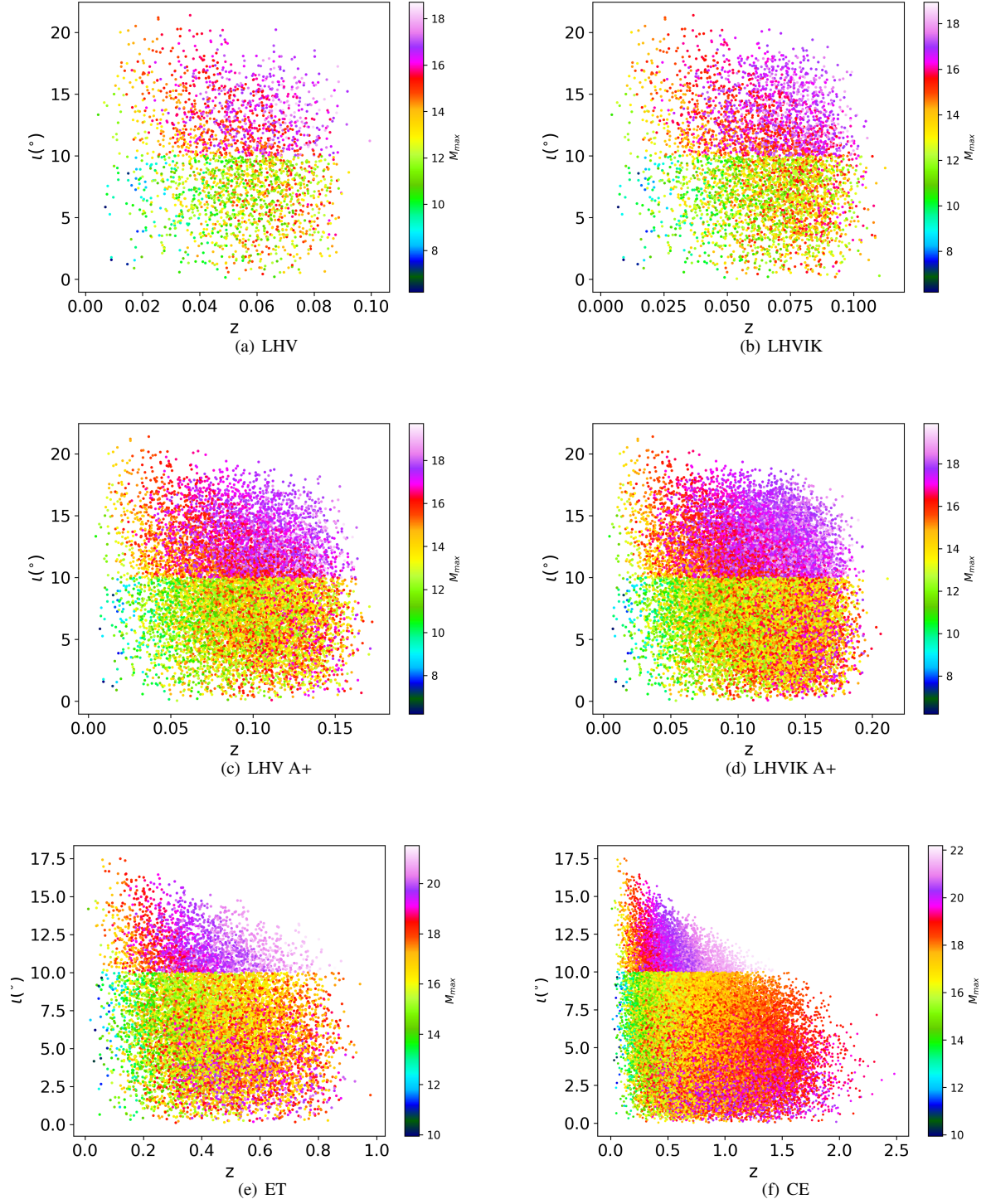


FIG. 3.— These figures show the distributions of ι , redshift of BNS samples and their afterglows flux, which can be triggered by GW detectors and GECAM. The upper and middle four panels with 2G GW detector networks LHV, LHVIK, LHV A+, LHVIK A+, show the results of 10^7 samples with $z \in (0, 0.3]$. The lower panels with ET and CE show the results of 10^7 samples with $z \in (0, 3]$. The colorbars show their R band magnitude of afterglows with $\theta_j = 10^\circ$.

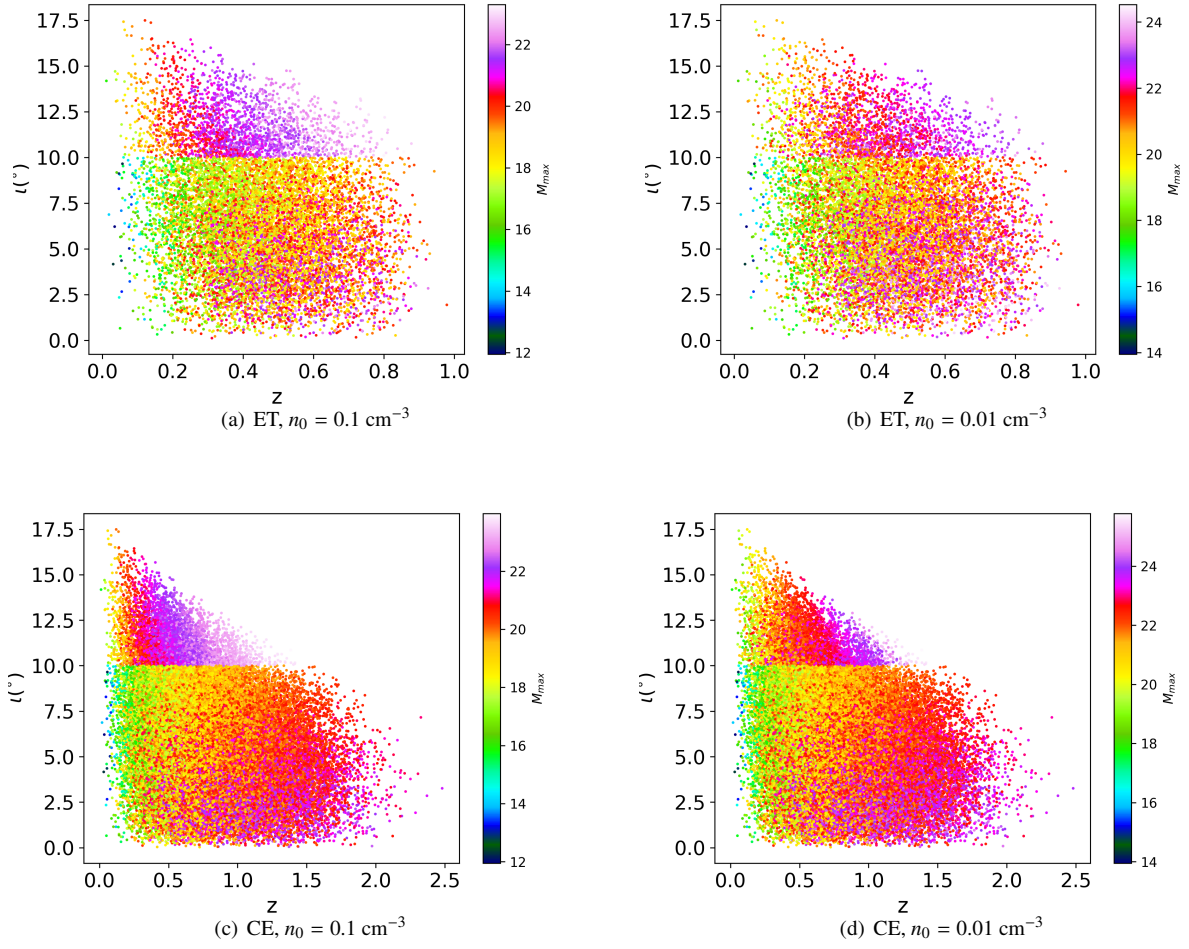


FIG. 4.— The same with Fig. 3, but with a different number density of the ISM. The left two panels show the results with $n_0 = 0.1 \text{ cm}^{-3}$ and the right panels show the result with $n_0 = 0.01 \text{ cm}^{-3}$.

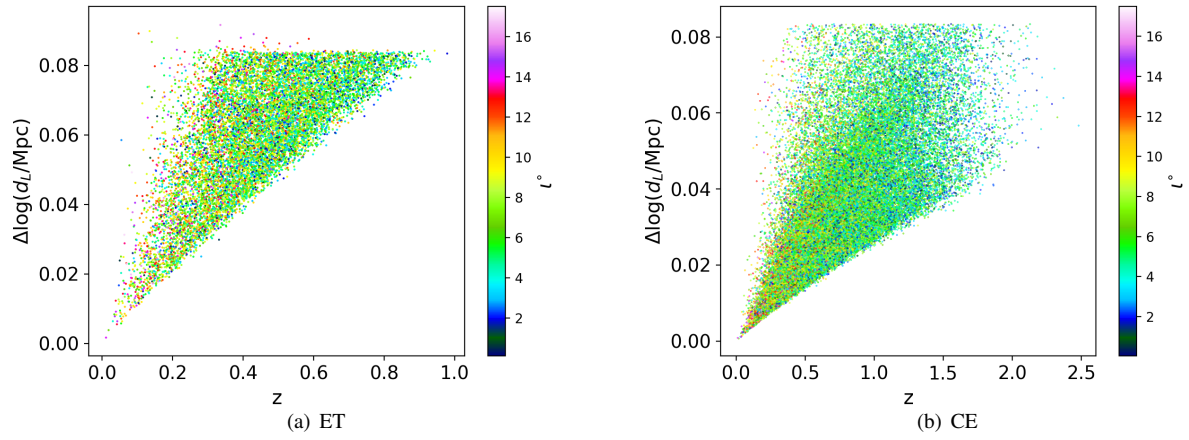


FIG. 5.— The distribution of samples' Δd_L and redshift, which can be triggered by 3G interferometers and GECAM. The left, right panels are the results with ET and CE, respectively. The color bar shows the samples' inclination angle.

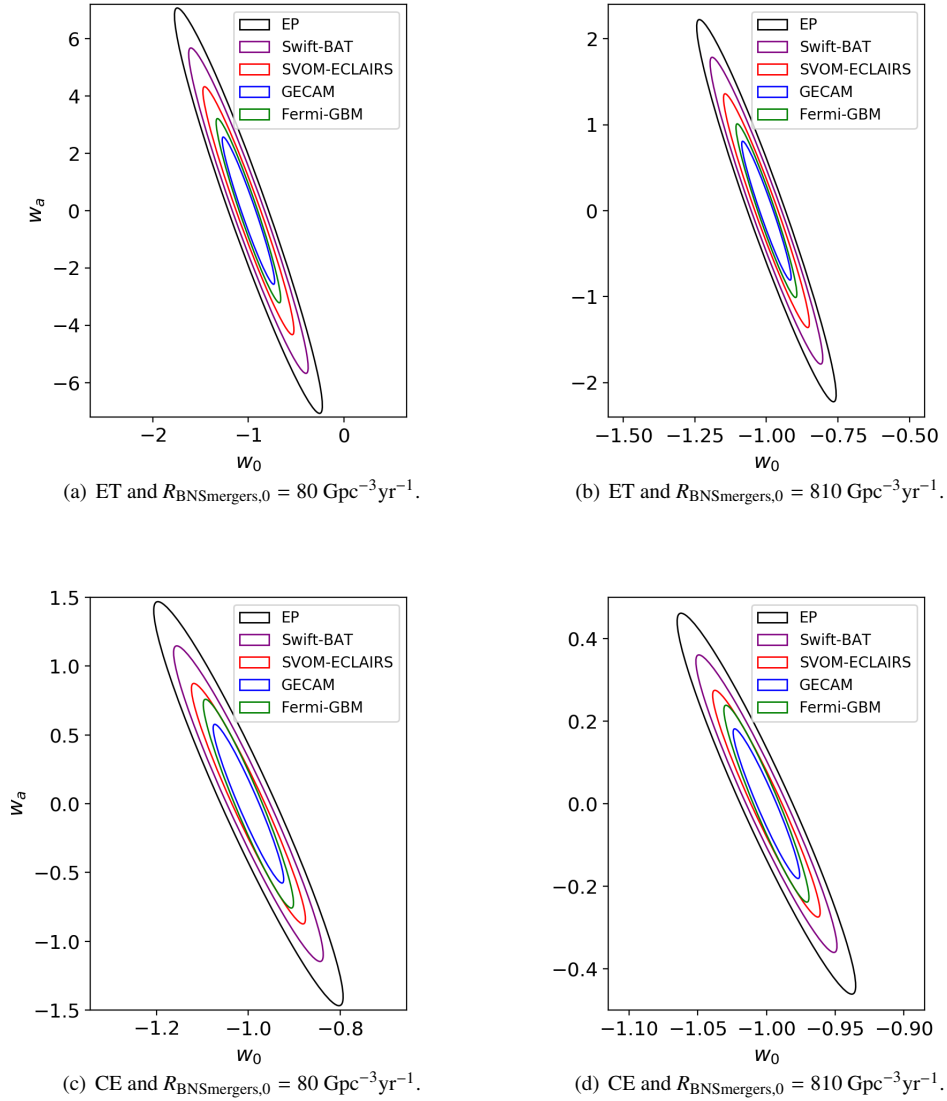


FIG. 6.— The two-dimensional uncertainty contours of the dark energy parameters w_0 and w_a for one year’s multi-messenger observation of ET, CE and five γ -ray detectors with a 68.3% ($1 - \sigma$) confidence interval. The left panels are the results with $R_{\text{BNSmergers},0} = 80 \text{ Gpc}^{-3}\text{yr}^{-1}$ and the right panels are the results with $R_{\text{BNSmergers},0} = 810 \text{ Gpc}^{-3}\text{yr}^{-1}$.

| | Swift-BAT | SVOM-ECLAIRS | GECAM | Fermi-GBM | EP |
|----------|-------------|--------------|--------------|--------------|-------------|
| LHV | 0.185-1.873 | 0.318-3.226 | 0.384-3.884 | 0.183-1.850 | 0.055-0.561 |
| LHVIK | 0.315-3.194 | 0.543-5.500 | 0.580-5.868 | 0.290-2.936 | 0.075-0.760 |
| LHV A+ | 0.529-5.356 | 0.911-9.222 | 1.007-10.198 | 0.563-5.702 | 0.117-1.186 |
| LHVIK A+ | 0.791-8.011 | 1.362-13.795 | 1.680-17.015 | 1.018-10.305 | 0.187-1.890 |
| ET | 8.8-89.3 | 15.2-153.7 | 44.3-448.3 | 29.2-259.2 | 5.3-54.0 |
| CE | 45.1-457.0 | 77.7-786.9 | 202.1-2046.3 | 122.3-1228.7 | 29.5-298.4 |

TABLE 3
THE SAME WITH TABLE 1, BUT WITH THE JET PROFILE IN TAN & YU (2018).

| | Swift-BAT | SVOM-ECLAIRS | GECAM | Fermi-GBM | EP |
|----------|--------------|--------------|--------------|--------------|-------------|
| LHV | 0.041-0.411 | 0.070-0.708 | 0.265-2.681 | 0.189-1.916 | 0.028-0.287 |
| LHVIK | 0.082-0.829 | 0.141-1.427 | 0.528-5.347 | 0.376-3.810 | 0.057-0.577 |
| LHV A+ | 0.208-2.112 | 0.359-3.636 | 1.308-13.239 | 0.922-9.332 | 0.142-1.444 |
| LHVIK A+ | 0.432-4.373 | 0.744-7.531 | 2.660-26.938 | 1.856-18.797 | 0.293-2.970 |
| ET | 18.3-185.7 | 31.5-319.8 | 85.0-860.7 | 53.0-536.2 | 11.5-116.4 |
| CE | 130.2-1318.2 | 224.2-2268.9 | 423.4-4287.4 | 227.4-2303.0 | 75.9-768.9 |

TABLE 4
THE SAME WITH TABLE 1, BUT WITH A GAUSSIAN TIME DELAY MODEL.

| | Swift-BAT | SVOM-ECLAIRS | GECAM | Fermi-GBM | EP |
|----------|-------------|--------------|--------------|--------------|-------------|
| LHV | 0.079-0.800 | 0.136-1.378 | 0.506-5.129 | 0.360-3.648 | 0.054-0.551 |
| LHVIK | 0.163-1.655 | 0.281-2.850 | 1.033-10.461 | 0.730-7.392 | 0.112-1.132 |
| LHV A+ | 0.421-4.264 | 0.725-7.343 | 2.563-25.944 | 1.780-18.021 | 0.284-2.878 |
| LHVIK A+ | 0.881-8.917 | 1.516-15.354 | 5.260-53.257 | 3.612-36.572 | 0.590-5.978 |
| ET | 27.3-276.2 | 47.0-475.7 | 119.4-1209.0 | 71.6-724.6 | 16.9-171.4 |
| CE | 90.6-917.4 | 156.0-1579.7 | 318.2-3221.7 | 176.0-1781.6 | 53.8-545.0 |

TABLE 5
THE SAME WITH TABLE 1, BUT WITH A FLAT MASS DISTRIBUTION BETWEEN $1 M_{\odot}$ AND $2.5 M_{\odot}$.

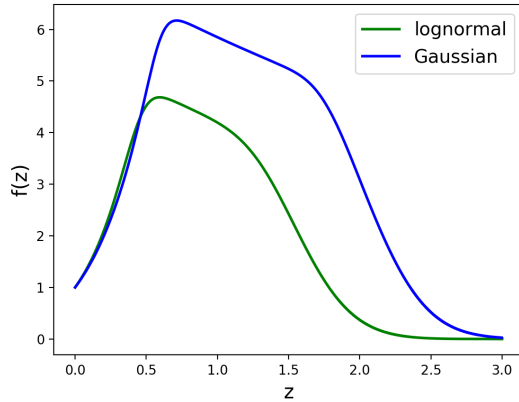


Fig. 7.— The redshift distribution of BNS merger samples. The green and blue lines represent the log-normal and Gaussian time delay models, respectively.

Central Universities under Grant Nos: WK2030000036 and WK3440000004.

REFERENCES

- Abbott, B. P., Abbott, R., Abbott, T. D., et al. 2016, *Phys. Rev. Lett.*, 116, 061102
- Abbott, B. P., Abbott, R., Abbott, T. D., et al. 2016, *Phys. Rev. Lett.*, 116, 241103
- Abbott, B. P., Abbott, R., Abbott, T. D., et al. 2016, *Phys. Rev. D*, 93, 122003
- Abbott, B. P., Abbott, R., Abbott, T. D., et al. 2016, *Phys. Rev. X*, 6, 041015
- Abbott, B. P., Abbott, R., Abbott, T. D., et al. 2017, *Phys. Rev. Lett.*, 118, 221101
- Abbott, B. P., Abbott, R., Abbott, T. D., et al. 2017, *Phys. Rev. Lett.*, 119, 141101
- Abbott, B. P., Abbott, R., Abbott, T. D., et al. 2017, *Phys. Rev. Lett.*, 119, 161101
- Abbott, B. P., Abbott, R., Abbott, T. D., et al. 2017, *Astrophys. J. Lett.*, 848, L12
- Abbott, B. P., Abbott, R., Abbott, T. D., et al. 2017, *Astrophys. J. Lett.*, 848, L13
- Abbott, B. P., Abbott, R., Abbott, T. D., et al. 2017, *Class. Quant. Grav.*, 34, 044001
- Abbott, B. P., Abbott, R., Abbott, T. D., et al. 2018, *Living Reviews in Relativity*, 21, 3
- Abbott, B. P., Abbott, R., Abbott, T. D., et al. 2019, *Phys. Rev. X*, 9, 031040
- Abbott, B. P., Abbott, R., Abbott, T. D., et al. 2020, *Astrophys. J. Lett.*, 892, L3
- Abbott, R., Abbott, T. D., Abraham, S., et al. 2020, *Astrophys. J. Lett.*, 896, L44
- Abbott, R., Abbott, T. D., Abraham, S., et al. 2020, *Phys. Rev. Lett.*, 125, 101102
- Abbott, R., Abbott, T. D., Abraham, S., et al. 2020, arXiv preprint arXiv:2010.14527
- Abbott, R., Abbott, T. D., Abraham, S., et al. 2020, arXiv preprint arXiv:2010.14533
- Abernathy, M., Acernese, F., Ajith, P., et al. Einstein gravitational wave Telescope conceptual design study[J]. 2011.
- Albrecht, A., Bernstein, G., Cahn, R. et al., *Report of the Dark Energy Task Force*, arXiv:astro-ph/0609591.
- Alexander, K. D., Margutti, R., Blanchard, P. K., et al. 2018, *Astrophys. J.*, 863, L18
- Arcavi, I. 2017, *Nature*, 551, 64
- Belgacem, E., Dirian, Y., Foffa, S., et al. 2019, *JCAP*, 08, 015
- Berger, E. 2014, *Annu. Rev. Astron. Astrophys.*, 52, 43
- Blair, D., Ju, L., Zhao, C. N., et al. 2015, *Science China Physics, Mechanics & Astronomy*, 58, 120402
- Blanchet, L. 2002, *Living Reviews in Relativity*, 5, 3
- Blanchet, L., Faye, G., Iyer, B. R. & Jorget, B. 2002, *Phys. Rev. D*, 65, 061501
- Blanchet, L., Damour, T. & Esposito-Farese, G. 2004, *Phys. Rev. D*, 69, 124007
- Blanchet, L., Damour, T., Esposito-Farese, G. & Iyer, B. R. 2004, *Phys. Rev. Lett.*, 93, 091101
- Blanchet, L., & Iyer B. R. 2005, *Phys. Rev. D* 71, 024004
- Chen, H. Y., Fishbach, M., & Holz, D. E. 2018, *Nature*, 526, 545
- Chen, H. Y. 2020, *Phys. Rev. Lett.*, 125, 201301
- Chevallier, M., & Polarski, D. 2001, *Int. J. Mod. Phys. D*, 10, 213
- Chu, Q., Howell, E. J., Rowlinson, A., et al. 2016, *Mon. Not. Roy. Astron. Soc.*, 459, 121
- Copeland, E. J., Sami M. & Tsujikawa, S., 2006, *Int. J. Mod. Phys. D*, 15, 11
- Coulter, D. A., Foley, R. J., Kilpatrick, C. D., et al. 2017, *Science*, 358, 1556
- Cutler, C., Apostolatos, T. A., Bildsten, L., et al. 1993, *Phys. Rev. Lett.*, 70, 2984.
- Damour, T., Jaranowski, P. & Schäfer, G. 2001, *Phys. Lett. B*, 513, 147
- Dwyer, S., Sigg, D., Ballmer, S. W., et al. 2015, *Phys. Rev. D*, 91, 082001
- Eichler, D., Livio, M., Piran, T. & Schramm, D. N. 1989, *Nature*, 349, 126
- Eisenstein, D. J., Zehavi, I., Hogg, D. W., et al. 2005, *Astrophys. J.*, 633, 560
- Erratum *ibid.* D, 71, 129902 (2005)
- Essick, R., Vitale, S. & Evans, M. 2017, *Phys. Rev. D*, 96, 084004
- Evans, P. A., Cenko, S. B., Kennea, J. A., et al., 2017, *Science*, 358, 1565
- Fishbach, M., Gray, R., Hernandez, I. M., et al. 2019, *Astrophys. J. Lett.*, 871, L13
- Granot, J., Panaitescu, A., Kumar, O., & Woosley, S. E. 2002, *Astrophys. J.*, 570, L61
- Gehrels, N., Chincarini, G., Giommi, P., et al. 2004, *Astrophys. J.*, 611, 1005
- Ghirlanda, G., Salafia, O. S., Paragi, Z., et al. 2019, *Science*, 363, 968
- Goldstein, A., Veres, P., Burns, E., et al. 2017, *Astrophys. J. Lett.*, 848, L14
- Götz, D., Osborne, J., Cordier, B., et al. 2014, *Proc. SPIE*, 9144, 914423
- Gray, R., Hernandez, I. M., Qi, H., et al. 2020, *Phys. Rev. D*, 101, 122001
- Gupta, A., Fox, D., Sathyaprakash, B. S. & Schutz, B. F., 2019, *Astrophys. J.*, 886, 71
- Hicken, M., Wood-Vasey, W. M., Blondin, S., et al. 2009, *Astrophys. J.*, 700, 1097
- Holz, D. E., & Hughes, S. A. 2005, *Astrophys. J.*, 629, 15
- Ioka, K., & Nakamura, T. 2019, *Mon. Not. Roy. Astron. Soc.*, 487, 4884
- Itoh, Y., Futamase T., & Asada, H. 2001, *Phys. Rev. D*, 63, 064038
- Itoh, Y. & Futamase, T. 2003, *Phys. Rev. D*, 68, 121501
- Itoh, Y. 2004, *Phys. Rev. D*, 69, 064018
- Itoh, Y. 2004, *Class. Quant. Grav.* 21, S529
- Ivezić, Ž., Kahn, S. M., Tyson, J. A., et al. 2019, *Astrophys. J.*, 873, 111
- Jaranowski, P., Krolak, A. & Schutz, B. F. 1998, *Phys. Rev. D*, 58, 063001
- Kilbinger, M., Benabed, K., Guy, J., et al. 2009, *A&A*, 497, 677
- Kiziltan, B., Kottas, A., De Yoreo, M., & Thorsett, S. E. 2013, *Astrophys. J.*, 778, 66
- Komatsu, E., Dunkley, J., Nolta, M. R., et al. 2009, *Astrophys. J. Suppl. Ser.*, 180, 330
- Kowalski, M., Rubin, D., Aldering, G., et al. 2008, *Astrophys. J.*, 686, 749
- Lazzati, D., Deich, A., Morsony, B. J., & Miller, M. C. 2017, *Mon. Not. Roy. Astron. Soc.*, 471, 1652
- Lazzati, D., Perna, R., Morsony, B. J., et al. 2018, *Phys. Rev. Lett.*, 120, 241103
- LIGO Scientific Collaboration 2016, *The LSC-Virgo White Paper on Instrument Science (2016-2017 edition)*

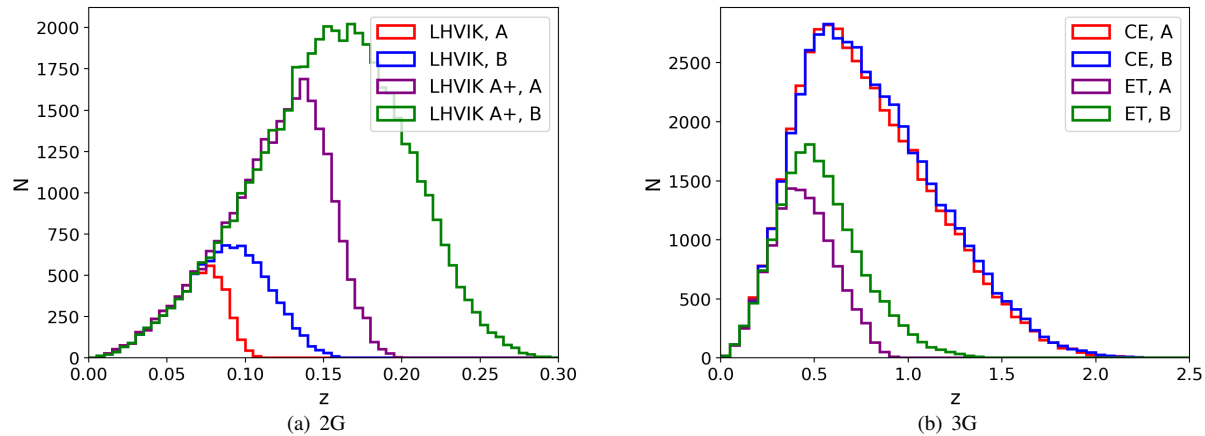


Fig. 8.— The comparison of two distributions of BNS mass. Model A represents the normal distribution mentioned in Sec. 2 and model B represents the flat mass distribution mentioned in Abbott et al. (2020e).

- LIGO Scientific Collaboration, Virgo Collaboration, IM2H Collaboration, et al. 2017, *Nature*, 551, 85
- LIGO Scientific, Virgo, Fermi GBM, INTEGRAL, IceCube, IPN, Insight-Hxmt, et al. 2017, *Astrophys. J. Lett.*, 848, L12
- Li, L. X., & Paczyński, B. 1998, *Astrophys. J. Lett.*, 507, L59
- Meegan, C., Lichti, G., Bhat, P. N., et al. 2009, *Astrophys. J.*, 702, 791
- Metzger, B. D. 2017, *Living reviews in relativity*, 20, 3
- Mészáros, P., & Martin J. R. 1999, *Mon. Not. Roy. Astron. Soc.*, 306, L39
- Mooley, K. P., Nakar, E., Hotokezaka, K., et al. 2018, *Nature*, 554, 207
- Mortlock, D. J., Feeney, S. M., Peiris, H. V., et al. 2019, *Phys. Rev. D*, 10, 103523
- Nakar, E., Piran, T., & Granot, J. 2002, *Astrophys. J.*, 579, 699
- Narayan, R., Paczynski B. & Piran T. 1992, *Astrophys. J. Lett.*, 395, L83
- Paczynski, B. 1986, *Astrophys. J. Lett.*, 308, L43
- Percival, W. J., Cole, S., Eisenstein, D. J., et al. 2007, *Mon. Not. Roy. Astron. Soc.*, 381, 1053
- Percival, W. J., Reid, B. A., Eisenstein, D. J., et al. 2010, *Mon. Not. Roy. Astron. Soc.*, 401, 2148
- Planck Collaboration, Ade, P. A. R., Aghanim, N., et al. 2016, *A&A*, 594, A13
- Preece, R. D., Briggs, M. S., Mallozzi, R. S., et al. 2000, *Astrophys. J. Suppl. Ser.*, 126, 19
- Punturo, M., Abernathy, M., Acernese, F., et al. 2010, *Class. Quant. Grav.*, 27, 194002
- Rosswog, S., 2005, *Astrophys. J.*, 634, 1202
- Rosswog, S., 2013, *Nature*, 500, 535
- Sari, R., Piran, T. & Narayan, J. P. 1998, *Astrophys. J.*, 497, L17
- Sathyaprakash, B. S. & Schutz, B. F. 2009, *Living Rev. Relativity*, 12, 2
- Sathyaprakash, B. S., Schutz, B. F., & Van Den Broeck, C. 2010, *Class. Quant. Grav.*, 27, 215006
- Savchenko, V., Ferrigno, C., Kuulkers, E., et al. 2017, *Astrophys. J. Lett.*, 848, L15
- Schrabback, T., Hartlap, J., Joachimi, B., et al. 2010, *A&A*, 516, A63
- Schutz, B. F., 1986, *Nature*, 323, 310
- Song H. R., Ai S. K., Wang M. H., et al. 2019, *Astrophys. J. Lett.*, 881, L40
- Soares-Santos, M., Holz, D. E., Annis, J., et al. 2017, *Astrophys. J. Lett.*, 848, L16
- Soares-Santos, M., Palmese, A., Hartley, W., et al. 2019, *Astrophys. J. Lett.*, 876, L7
- Sun, H., Zhang, B., & Li, Z. 2015, *Astrophys. J.*, 812, 33
- Tanvir, N. R., Levan, Astron. J., Gonzalez-Fernandez, C., et al. 2017, *Astrophys. J. Lett.*, 848, L27
- Tan, W. W. & Yu, Y. W. 2018, *Astrophys. J.*, 902, 83
- Tanvir, N. R., Levan, A. J., Fruchter, A. S., et al. 2013, *Nature*, 500, 547-549
- Troja, E., Piro, L., Ryan, G., et al. 2018, *Mon. Not. Roy. Astron. Soc.*, 487, L18
- Unnikrishnan, C. S. 2013, *Int. J. Mod. Phys. D*, 22, 1341010
- Virgili, F. J., Zhang, B., O'Brien, P. & Troja, E., 2011, *Astrophys. J.*, 727, 109
- Valenti, S., David, J., Yang, S., et al. 2017, *Astrophys. J. Lett.*, 848, L24
- Vitale, S. & Evans, M. 2017, *Phys. Rev. D*, 95, 064052
- Wanderman, D. & Piran, T. 2015, *Mon. Not. Roy. Astron. Soc.*, 448, 3026
- Wang, B., Zhu, Z. Y., Li, A. & Zhao, W., 2020, *Astrophys. J. Suppl. Ser.*, 250, 6
- Wang, Y. Y. & Wang, F. Y. 2019, *Astrophys. J.*, 873, 39
- Wen, L. & Chen, Y. 2010, *Phys. Rev. D*, 81, 082001
- Weinberg, S. 2008, *Cosmology*, Oxford University Press
- Yan, C. S., Zhao, W., & Lu, Y. J., 2020, *Astrophys. J.*, 889, 79
- Yonetoku, D., Murakami, T., Nakamura, T., et al. 2004, *Astrophys. J.*, 609, 935
- Yu, J. M., Wang, Y., Zhao, W. & Lu, Y. J. 2020, *Mon. Not. Roy. Astron. Soc.*, 498, 1786
- Yuan, W., Zhang, C., Chen, Y., et al. 2018, *Scientia Sinica Physica, Mechanica & Astronomica*, 48, 039502
- Yuksel, H., Kistler, M. D., Beacom, J. F., et al. 2008, *Astrophys. J.*, 683, L5
- Zhao, W., Wright, B. S. & Li, B., 2018, *JCAP*, 10, 052
- Zhao, W., van den Broeck, C., Baskaran, D., & Li, T. G. F. 2011, *Phys. Rev. D*, 83, 023005
- Zhao, W. & Santos, L. 2019, *JCAP*, 11, 009
- Zhao, W. & Wen, L. 2018, *Phys. Rev. D*, 97, 064031
- Zhang, B. & Mészáros, P. 2002, *Astrophys. J.*, 571, 876
- Zhang, X., Yu, J., Liu, T., Zhao, W. & Wang, A. Z. 2017, *Phys. Rev. D*, 95, 124008
- Zhang, D. L., Li, X. Q., Xiong, S. L., et al. 2018, arXiv preprint arXiv:1804.04499
- Zhang, G. Q. & Wang, F. Y. 2018, *Astrophys. J.*, 852, 1
- Zou, Y. C., We, X. F. & Dai, Z. G. 2007, *Astron. Astrophys.*, 461, 115

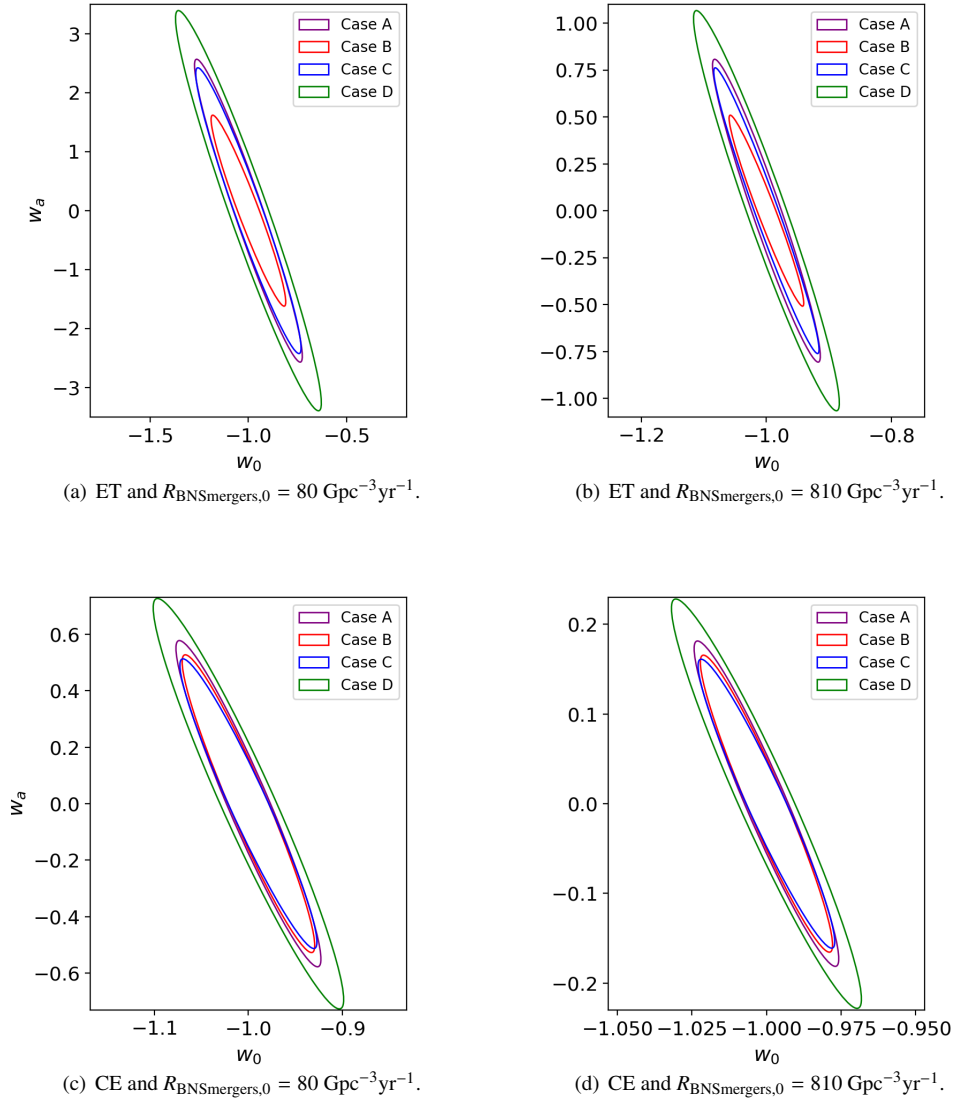


FIG. 9.— The two-dimensional $1\text{-}\sigma$ uncertainty contours of the dark energy parameters w_0 and w_a with different BNS samples. Case A represents the results of delay time with lognormal distribution and a Gaussian BNS mass distribution, case B uses a flat mass distribution, case C uses Gaussian delay time model and case D uses two-Gaussian jet profile.